

Development and Validation of an Integrated EV Charging Station with Fuzzy Logic Controlled Grid-Interfacing Inverter for Residential Applications

Nambaru Pavan Kumar¹, CH. Vishnu Chakravarthy²

¹M.Tech(PSA), EEE, Sanketika vidya parishad engineering college., India

²Assistant Professor, EEE, Sanketika vidya parishad engineering college., India

E-mail: [1pavankumarnambaru65@gmail.com](mailto:pavankumarnambaru65@gmail.com), [2vishnu.chakravarti@gmail.com](mailto:vishnu.chakravarti@gmail.com)

ABSTRACT:

This work proposes a new fuzzy logic controller-based grid-connected modular inverter for a residential integrated bidirectional charging station. By boosting the grid's stability and offering buffering services, the technology is intended to sustain the electrical grid. The proposed arrangement consists of a modular, bidirectional inverter with EV charging capabilities. The system can operate in multiple modes, including EV battery charging and discharging, grid energy storage during low-demand times, and grid energy delivery during high-demand times. The development of a low-level control approach to regulate power flow between the EV battery, household load, and the grid is based on the droop control technique and feedforward decoupling, enhanced by fuzzy logic. The performance of the proposed system is assessed using MATLAB/Simulink software simulation experiments. The outcomes demonstrate how effectively the system integrates renewable energy sources and sustains the grid during periods of high demand. Increased reliability is also achieved through its backup power supply function during blackouts. An 87% charging efficiency with a 35% SoC and 6.3 kW of grid power is confirmed by an experimental validation conducted in a lab setting. With a 55% SoC, returning power to the grid produces an 8.6 kW AC output and an 8.77 kW battery input, resulting in a V2G efficiency of about 94%. The integration of fuzzy logic control enhances the system's performance, making it a promising solution for intelligent and sustainable energy systems.

1. INTRODUCTION:

The automobile industry is currently undergoing a transformation due to increased demand for alternatives to oil, which remains the main energy source for transportation, and concerns about climate change.[1] Rising energy prices in Europe are also driving concerns

The literature suggests that the best way to charge an electric vehicle (EV) at home with up to 11kW of charging power is to use Level 2 charging with an AC electric vehicle service equipment (EVSE) outlet.[4] Typically, this involves the vehicle's on-board charging (OBC) system, which has its own capacity and space limitations. However, the direct grid connectivity of the EVSE wall box for AC charging makes it susceptible to current imbalance. Additionally, due to the PWM communication protocol, this device cannot retrieve information on EV batteries, which is a primary disadvantage of the typical AC charging wall box.[5]

Conversely, Europe has seen a surge in the use of Renewable Energy Sources (RESs) in recent years. It is projected that by 2030, the percentage of solar energy used in power production capacity will rise from 33% to 67%, with over half of that energy coming from rooftop installations. By 2022–2023, nearly one million homes in Europe are expected to be powered by solar energy. These homes consume an average of 10 to 15 kWh of energy each day. By incorporating a fuzzy logic controller, these systems can be enhanced for better performance and efficiency. [6]A fuzzy logic controller can manage the charging process more dynamically and

efficiently by considering various parameters and uncertainties, such as fluctuating energy availability from RESs and varying household energy demands. This approach helps to mitigate issues like current imbalance and improves overall energy management, making home EV charging more reliable and sustainable in the context of increasing RES integration.[7]

Therefore, a normal car battery with a capacity of between 30 and 100 kWh, when completely charged, may be able to supply the necessary electricity to a home during an emergency for a few days. To connect the battery energy source system (BESS), [8] EV battery, and renewable energy sources (RESs) to the household loads, this solution calls for a smart interface hub. Regrettably, the AC charging EVSE cannot be upgraded to incorporate RESs into the charging process. A workable option for this kind of smart interface hub are DC charging stations.

Residential DC charging stations for electric vehicles are capable of producing DCs up to 22 kW in maximum power, more than twice as fast as an average wall box running on AC [9], [10]. Consequently, one of the primary problems with EV charging at the moment is the lengthy charging process. This can be greatly decreased with a DC charging infrastructure. Nowadays, bidirectional DC charging station technology is far more reliable. A thorough analysis of the state-of-the-art in DC charging systems is conducted in [11], covering both practical energy storage projects that are being implemented globally and contributions made by academic researchers.

There has been a surge in research interest in off-grid (standalone mode) and hybrid (able to operate in both grid-connected and standalone modes) EV charging systems [12]. Additionally, research is done on the economic evaluation of DC charging solutions. By lowering grid dependency and system reliability, the V2G facility advantages homeowners with private power production mix technologies in terms of Total Cost of Ownership (TCO). An 8X150Ah lithium-ion battery is needed

for a standard 10kW solar house system, which makes up 10% of the total cost of ownership [13].

According to recent research, battery buffering in conjunction with DC charging technology for EVs has the ability to successfully meet the rising demand for EV charging and save network operators' total cost of ownership (TCO) by as much as 30% [14]. In [15], a thorough TCO analysis of V2G service is carried out for several charge models, including private, semi-public, and public. In comparison to AC charging using a wall box, DC charging solutions for private homes can offer homeowners a lower total cost of ownership. Nevertheless, the majority of the research that was done was on high-power DC charger technologies for parking lots and public areas. There is a dearth of study on the feasibility analysis of home DC charging, including suitable communication protocols.

As a result, DC charging solutions for individual homes can allow owners more control over their power source and affordable electricity. This research effort is unusual in that it presents a novel system that incorporates system modelling, control, and validation for the purpose of integrating an EV charging station with a grid-interfacing inverter to buffer the energy supply system (ESS) for residential applications.

The researchers focus on the bidirectional DC charging station, which can use the RES to reduce the homeowner's energy costs in addition to charging EVs during off-peak hours.

Type 2 connection interface. For this effort, the hardware design specifics are not the main focus. The charging and discharging process uses the ISO 15118-20 communication protocol. With MATLAB/Simulink 2019b, a comprehensive state space modelling of the parallel DC/AC converter system is created. The suggested method has also been experimentally validated, demonstrating its efficacy in delivering dependable and efficient charging services with the least possible negative grid impact.

All things considered, this research helps to create intelligent and ecological ways to charge electric cars. The remainder of the work is structured in this manner. The concept of a grid-connected inverter integrated DC charging system for domestic use was covered in Section II along with the required figures. In Section III, state equations in a synchronous reference frame were used to generalise state-space modelling for parallel linked DC/AC converters. The control techniques used for charging, as well as the V2G and V2H modes of operation, are described in Section IV. The simulation findings for each use case scenario were covered in Section V. Section VI contains the final presentation of the conclusions.

II. The concept of a DC charging station integrated with a grid-connected inverter. Figure 1 depicts a traditional power generation mix system for residential usage. The main component of this system is the 10-kW grid-tied inverter, which supplies the DC power from 10 kWp solar PV to the wall box that powers the electric car charger and the household load [18], [19].

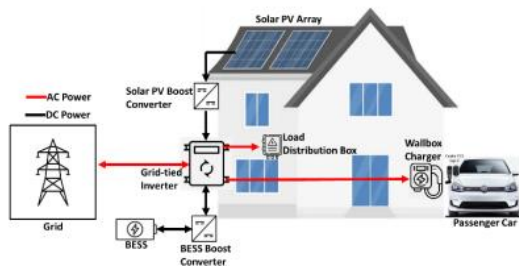


FIGURE 1. traditional power production mix that includes grid, BESS, and solar PV for household load delivery and EV charging

The average monthly household load consumption in Belgium is 20 kWh, equivalent to the power used by a family of four people. Based on this usage, a battery size of 66 kWh, providing two days of autonomy, is necessary. Additionally, the wall box charger uses AC power to charge the EV up to 7.4 kW for private car garages using an on-board charger (OBC).[20] The Volkswagen ID Buzz electric vehicle, with its 77kWh battery and 350V

battery voltage, requires approximately 10.5 solar photovoltaic and battery energy storage systems (BESS) with smart charging is not possible with the traditional AC wall box charger. By incorporating a fuzzy logic controller and combining it with a grid-tied inverter suitable for a bidirectional DC charging station with a COMBO CCS type 2 charging connection, these shortcomings of the traditional AC wall box EVSE system can be addressed. The consumption. This integration enables not only efficient charging but also V2G capabilities, allowing for bidirectional power transfer. Hours to charge. Furthermore, because the conventional OBC of the vehicles is unidirectional, the wall box charger does not provide V2G service. The AC wall box system typically uses the OCPP 1.6j communication protocol, which does not permit bidirectional power transfer. Moreover, the integration of fuzzy logic controller can optimize the charging process by dynamically managing power flow and adapting to real-time conditions, such as varying solar energy availability and household energy. It also facilitates the seamless integration of solar PV and BESS, enhancing the overall efficiency and sustainability of the EV charging system.

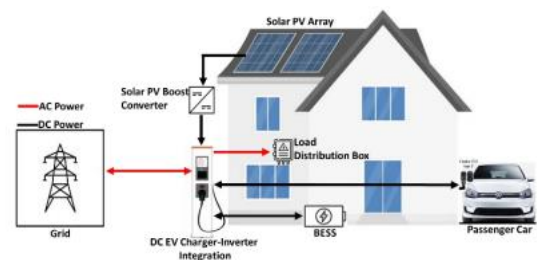
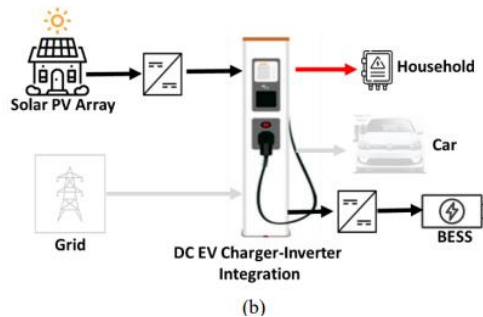


FIGURE 2 EV charging and household load supply from solar PV, BESS, and the grid are included in the proposed integrated DC charger with grid-connected inverter system.

Figure 2 depicts the total power generating mix system architecture with grid-connected inverter integration and integrated DC EV charger. Via a Combo CCS Type 2 charging connector, the suggested system can provide V2G service and bidirectional up to 22kW DC charging at home. Additionally, the EV battery can be used by the

system as energy reserve for household use in case of emergency and/or nightly routine power backup. On hot summer days, a large portion of the energy mix comes from solar power, which can be used to meet household load demand and either transmit excess energy to the home BESS for charging or In this instance, the typical battery sizing estimate for a solar home system can be used to lower the size of the BESS [18].

The innovation of this research is summed up in TABLE I, which shows how the novel approach suggested can improve the conventional system to a certain extent. The suggested system operation mode is contingent upon the availability of solar irradiance, the state-of-charge (SoC) of EV batteries, the SoC of BESS, and the cost of energy. Figure 3 shows the suggested system's operational modes. In order to comprehend how the suggested system operates, it is assumed that the EV stays at home between 11 p.m. and 6 a.m., or off-peak hours, when energy costs are lowest.



Since there isn't any solar power generated during these hours, as Figure 3(a) illustrates, the EV charges using less expensive electricity from the grid. The grid can also supply the household load requirement. Around 95% SoC is produced by the sun's rays during peak hours (7 a.m. to 4 p.m.), when EVs are not in the office. As seen in Figure 3(b), the integrated charging station operates in both islanding and off-grid inverter modes to meet residential loads and store extra energy for the BESS system or return it to the grid. When the EV returns home with about 60% SoC in the evening (5:00–11.00 pm), the suggested system operates in V2H mode.

As demonstrated in Figure 3(c), the needed household load demand in the evening can be satisfied by combining the use of the BESS and EV battery storage. It usually takes the homeowner's permission to activate the V2G mode due to significant fluctuations in frequency and voltage. In order to transfer battery power to the grid, the suggested system operates in grid-connected mode in this manner. The BESS can supply the domestic load, as Figure 3(d) illustrates.

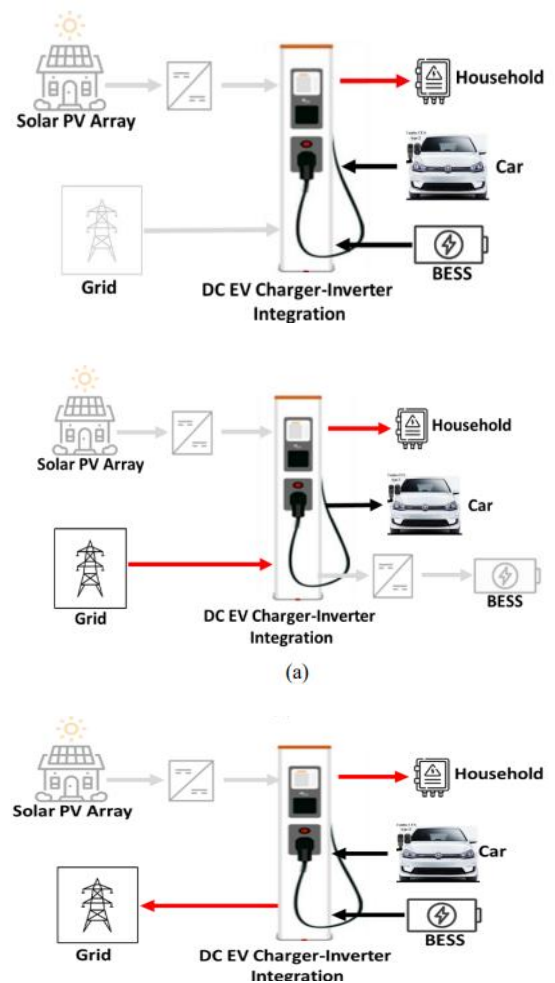


FIGURE 3. Various modes of operation for an integrated DC charging station with an inverter connected to the grid. (a) EV Charging mode

III. Parallel grid-connected DC/AC converter generalized state-space modelling:

If a charging station with numerous AC/DC converter modules connected in parallel with an LCL filter is depicted in Figure 5, a fuzzy logic

controller can be integrated to enhance performance. A damping resistor, R_d , is attached to each filter's filter capacitors, C_f . The model considers the three-phase converter- and grid-side inductors, L_c and L_g , respectively, and their mutual coupling terms, M_{cg} and M_{gc} , converter-to-grid side and converter-to-converter side. These coupling factors are often disregarded, even when one inductor per phase is substituted by a three-phase inductor. The three-phase inductors significantly impact the system's dynamic response, making it essential to account for them. The grid inductance, L , is also included in the model. By incorporating a fuzzy logic controller, the charging station can dynamically manage the interactions between the various components, such as the three-phase inductors and the damping resistors. The fuzzy logic controller can adaptively adjust the control parameters in real-time, ensuring optimal performance and stability despite the complexities introduced by the coupling factors. This approach improves the system's dynamic response and overall efficiency, leading to a more robust and reliable charging station design.

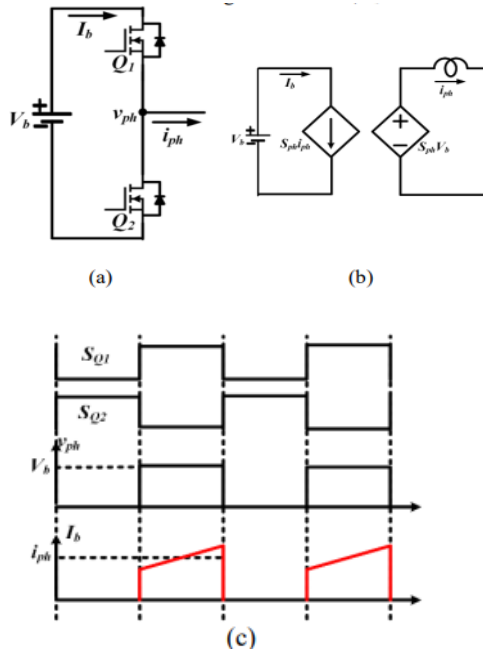


FIGURE 4. A half-bridge switch module with switching behaviour represented by a small signal average model. (a). Half-bridge model, (b). Small signal model for half bridge, (c) Waveform

of voltage and current with half bridge module switching signal

An averaged model of the parallel V2G converters with n number module in the stationary three-phase frame may be derived from the tiny signal equivalent circuit of each half-bridge module with switching characteristics, as illustrated in Figure 4. I_{gx} stands for the grid-side currents, and I_{cx} for the converter-side currents. The symbol I_{sx} represents the grid source currents. Keep in mind that the notation x represents the a, b, and c phases. Furthermore, the synchronous reference frame's three-phase leg's duty cycle, designated as S_a , S_b , and S_c . The input and state matrices make up the state space model of the n parallel V2G charger module.

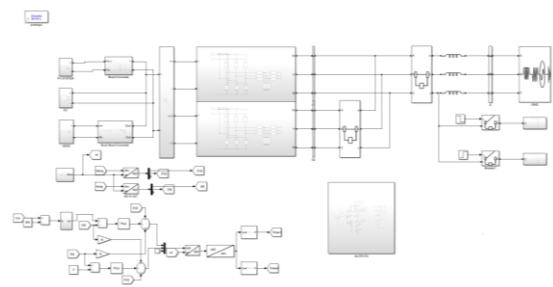


FIGURE 5. An isolator switch connects the controller to the grid and the house load, and a modular bidirectional AC/DC converter with an LCL filter

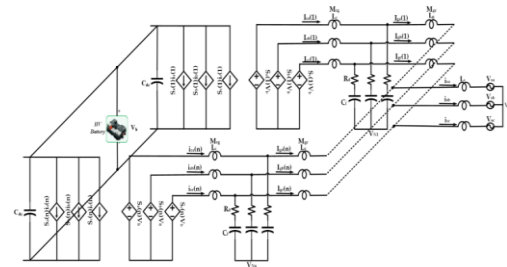


FIGURE 6A parallel AC/DC converter module with an LCL filter using a small signal average model.

For this study project, two converters are taken into consideration. The dynamic equation for each of the system's state variables can be used to generate these matrices. Using the method

outlined in [21]– [22], the state equations of a bidirectional parallel converter system can be written. The LCL filter in this system is primarily responsible for the system's dynamic performance. As a result, the voltage across the filter capacitor and the inductor currents constitutes the system's state variables. The expression in (1) for the state variables of n parallel V2G converter systems has the superscripts "c" and "g" standing for the converter and grid sides, respectively.

Furthermore, the filter is indicated by the superscript "f". The duty cycles in the synchronous reference frame (SRF) serve as the input variables are articulated in (2). The model's state and input equations in the SRF frame are derived from (3), where the input vector U comprises disturbances (the d and q terms of the grid voltage) as well as control variables (the duty cycles of each inverter leg).

The auxiliary matrices, A, B, C, and D, can be created using the state variables' dynamic equation. We can assume that the charger system has been configured using an SRF, in which the grid voltage is aligned to the d-axis, in order to calculate the simplified dynamic equations. With this configuration, the reactive power may be controlled using the q-axis current, while the active power can be independently adjusted using the d-axis current.

$$X = Y = \begin{bmatrix} i_d^c(1), i_q^c(1), i_0^c(1), i_d^g(1), i_q^g(1), i_0^g(1) \dots \dots \dots \\ i_d^c(n), i_q^c(n), i_0^c(n), i_d^g(n), i_q^g(n), i_0^g(n) \\ \dots \dots \dots v_d^f(1), v_q^f(1), v_0^f(1), \dots \dots \dots \\ v_d^f(n), v_q^f(n), v_0^f(n) \end{bmatrix}^T \quad (1)$$

$$U = \begin{bmatrix} s_d(1), s_q(1), s_0(1) \dots \dots \dots \\ s_d(n), s_q(n), s_0(n) \\ v_d^g, v_q^g, v_0^g \end{bmatrix}^T \quad (2)$$

$$\frac{d}{dt} X = AX + BU \quad (3)$$

$$Y = CX + DU$$

The zero-sequence component, or 0-axis current, can also be changed to regulate the circulating current. In (4) through (6), the state equations are displayed. Here, $[xdq0 \ c(k)] = [id \ c \ vq \ c \ v0] \ T$ denotes the voltage and currents of the converter-

side inductor, and $[xdq0 \ g(k)] = [id \ b \ vc \ vx \ v0 \ g] \ T$ for the grid-side inductance. In a similar vein, the voltage across the filter capacitor is expressed by $[Vdq0(k)] = [vd \ f \ vq \ v0] \ T$.

The dynamic equation for the output voltage is displayed in equation (7), where Vb and Ib stand for the voltage and current of a battery. The conversion matrix T, which is represented in equation (8), is utilised to transform the ABC frame into a dq frame that has grid angular frequency, τ . The T matrix is rewritten in terms of ω , which is given in (9), simplifying the dynamic equation. The converter identifications connected in parallel ($K = 1, 2, 3, n$) are indicated by the symbol k in these equations. The dynamic equations given above are carefully formulated to yield the auxiliary matrices A, B, C, and D. Appendix contains a discussion of the matrices

$$\frac{d}{dt} [x_{dq0}^c(k)] = -TdT^{-1}/dt [i_{dq0}^c(k)] + v_b I_{L1} [S_{dq0}(k)] - I_{L1} [v_{dq0}^f(k)] + R_d I_{L1} [i_{dq0}^c(k)] + R_d I_{L1} [i_{dq0}^g(k)] - \sqrt{3}(v_n^-, -v_n^-) I_{L1} [0 \ 0 \ 1] \quad (4)$$

$$\frac{d}{dt} [x_{dq0}^q(k)] = -T \frac{dT^{-1}}{dt} [i_{dq0}^g(k)] + I_{L2} [v_{dq0}^c(k)] + R_d I_{L2} [i_{dq0}^g(k)] - I_{L2} [v_{dq0}^s(k)] - \sqrt{3} (V_n^+ - V_n^-) I_{L2} [0 \ 0 \ 1] \quad (5)$$

$$\frac{d}{dt} [x_{dq0}^q(k)] = -T \frac{dT^{-1}}{dt} [i_{dq0}^g(k)] + I_{L2} [v_{dq0}^c(k)] + R_d I_{L2} [i_{dq0}^g(k)] - I_{L2} [v_{dq0}^s(k)] - \sqrt{3} (V_n^+ - V_n^-) I_{L2} [0 \ 0 \ 1] \quad (6)$$

$$d/dt V_b = 1/ [nC]_{dc} (I_b - [s_{dq0}(k)] * [i_{dq0}^c(k)]) \quad (7)$$

$$T = \sqrt{(2/3)} [\cos(\omega t) \ \cos(\omega t - 2\pi/3) \ \cos(\omega t + 2\pi/3) \ \omega t(\omega t - 2\pi/3)(\omega t + 2\pi/3) \ 1/\sqrt{2} \ 1/\sqrt{2} \ 1/\sqrt{2}] \quad (8)$$

$$T \left[\frac{dT}{dt} \right]^{(-1)} / dt = [0 \quad -\omega \quad 0 \quad \omega \quad 0 \quad 0 \quad 0 \quad 0] \tag{9}$$

IV. CONTROL STRATEGIES FOR PROPOSED INTEGRATED DC CHARGER-INVERTER SYSTEM:

Multimode operation is available for the proposed bidirectional EV charging station with buffered BESS support, as shown in Section II. During various operating modes, the station must maintain the bidirectional power flow. When using the EV battery to supply electricity, there are three different sorts of operation modes. When the EV battery is powering the household during an emergency, the converter must function in standalone mode by keeping the voltage and frequency constant.

Grid forming is another name for this phase, which is depicted in Figure 7(a). The output frequency is fixed, meaning that the converter determines it rather than the grid imposing it. As seen in Figure 7(b), the converter can also function in grid-connected mode, which equates to charging and discharging the EV battery from and to the grid. The AC/DC converter modifies its output when charging voltage depending on the input from the grid, enabling controlled power transfer to the battery. Grid following mode is

another name for this inverter operating mode. The DC/AC converter functions as an inverter to transform the DC power from the battery into AC power during discharge, also known as V2G mode. The grid-connected inverter then feeds the AC power back into the grid. To guarantee that the power transfer is in sync with the grid, the DC/AC inverter modifies its output voltage and frequency to correspond with the grid. The next subsections explain the charging, V2G, and V2H control methods. shows a charging station made up of several parallel-connected AC/DC converter modules.

A.OFF-GRID INVERTER MODE (V2H MODE):

Under grid forming mode control, the off-grid inverter produces a three-phase voltage with a consistent magnitude and frequency in this mode [23]. This mode supplies its own local load from renewable energy sources or energy storage devices when the home load is not connected to the main grid. The grid-connected inverter's full independent mode control is displayed in Figure 8. It is composed of a phase-locked loop (PLL) and dq transformation for an external three-phase signal, or double-loop control of the voltage and current control sections.

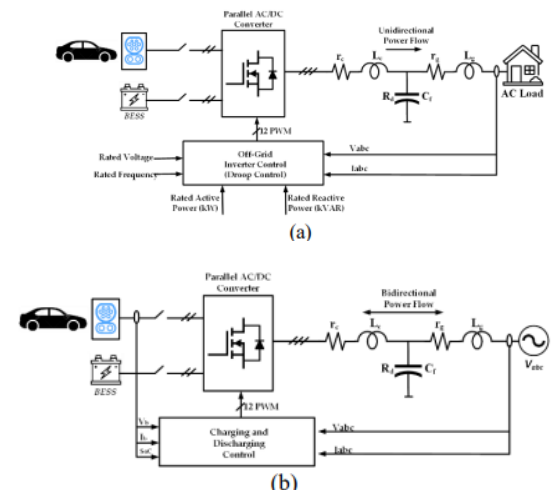


FIGURE 7. Proposed integrated charging station converter control strategies. (a) Off-grid inverter control for V2H mode; (b) Charging and discharging control for charging G2V and V2G mode. The voltage reference in terms of v_d and v_q is followed by the three-phase voltage produced by this system. The voltage (10) and frequency (11) references of the must be calculated.

The house load as shown in Figure 8, where V_{ref} and f_{ref} are voltage and frequency commands that depend on the chosen island mode, and P and Q are the (12) and (13), respectively, represent the measured active and reactive power. P_0 and Q_0 are the rated active and reactive power.

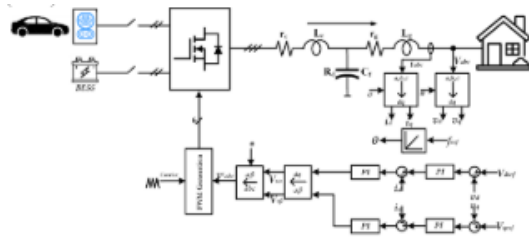


FIGURE 8. Off-grid inverter control to keep the household load's voltage and frequency stable

$$f_{ref} = f_0 - K_p(P - P_0) \quad (10)$$

$$V_{ref} = V_0 - K_q(Q - Q_0) \quad (11)$$

$$P = v_d i_d + v_q i_q \quad (12)$$

$$Q = v_d i_q + v_q i_d \quad (13)$$

Using equations (14) and (15), the droop characteristic constants, K_p (Hz/W) and K_q (Volt/VAR), are computed, where f_{max} and V_{max} are the maximum allowed frequency and voltage in the maximum active power and reactive power that can be transferred are island mode, P_{max} , and Q_{max} . The stability of the network is impacted by the choice of the droop constants, K_p and K_q . Broadly speaking, we can say that the system's stability margin decreases with increasing droop constant values

The controller modifies the position of the droop characteristic in response to a change in load in order to restore the rated voltage and frequency. The operating point is adjusted from A to B, increasing the voltage from V_{d0} to V_{d1} , and the conventional-droop mode is enabled, as shown in Figure 9, which also shows a reduction in the house reactive power demand from Q_0 to Q_1 .

To meet the lower reactive power requirement, the droop characteristic is adjusted, and the inverter's voltage reference shifts to V_{d0} . When the active power load varies, the frequency exhibits the same tendency. In this manner, (16) and (17) are used, respectively, to determine the voltage, V_{ref} , and frequency, f_{ref} .

A.OFF-GRID INVERTER MODE (V2H MODE):

Under grid forming mode control, the off-grid inverter produces a three-phase voltage with a consistent magnitude and frequency in this mode [23]. This mode supplies its own local load from renewable energy sources or energy storage devices when the home load is not connected to the main grid. The grid-connected inverter's full independent mode control is displayed in Figure 8. It is composed of a phase-locked loop (PLL) and dq transformation for an external three-phase signal, or double-loop control of the voltage and current control sections.

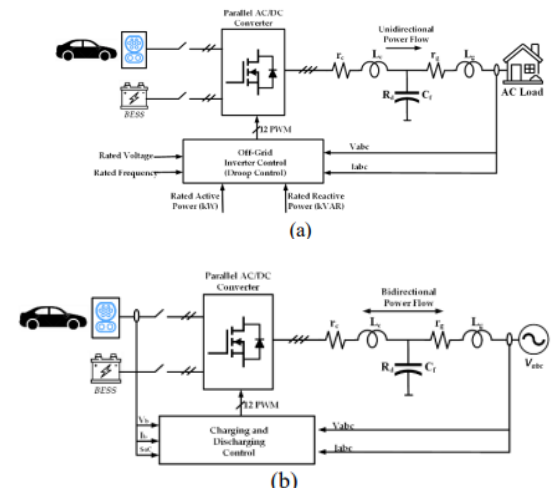


FIGURE 7. Proposed integrated charging station converter control strategies. (a) Off-grid inverter control for V2H mode; (b) Charging and discharging control for charging G2V and V2G mode the voltage reference in terms of v_d and v_q is followed by the three-phase voltage produced by this system. The voltage (10) and frequency (11) references of the must be calculated.

The house load as shown in Figure 8, where V_{ref} and f_{ref} are voltage and frequency commands that depend on the chosen island mode, and P and Q are the (12) and (13), respectively, represent the measured active and reactive power. P_0 and Q_0 are the rated active and reactive power.

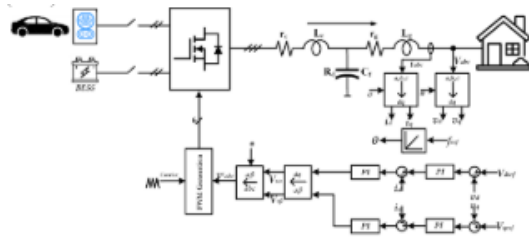


FIGURE 8. Off-grid inverter control to keep the household load's voltage and frequency stable

$$f_{ref} = f_0 - K_p(-P_0) \quad (10)$$

$$V_{ref} = V_0 - K_p(Q - Q_0) \quad (11)$$

$$P = v_d i_d + v_q i_q \quad (12)$$

$$Q = v_d i_q + v_q i_d \quad (13)$$

Using equations (14) and (15), the droop characteristic constants, K_p (Hz/W) and K_q (Volt/VAR), are computed, where f_{max} and V_{max} are the maximum allowed frequency and voltage in the maximum active power and reactive power that can be transferred are island mode, P_{max} , and Q_{max} . The stability of the network is impacted by the choice of the droop constants, K_p and K_q . Broadly speaking, we can say that the system's stability margin decreases with increasing droop constant values.

$$K_P = (f_{max} - f_0) / (P_{max} - P_0) \quad (14)$$

$$K_Q = (V_{max} - V_0) / (Q_{max} - Q_0) \quad (15)$$

The controller modifies the position of the droop characteristic in response to a change in load in order to restore the rated voltage and frequency. The operating point is adjusted from A to B, increasing the voltage from V_{d0} to V_{d1} , and the conventional-droop mode is enabled, as shown in Figure 9, which also shows a reduction in the house reactive power demand from Q_0 to Q_1 .

To meet the lower reactive power requirement, the droop characteristic is adjusted, and the inverter's voltage reference shifts to V_{d0} . When the active

power load varies, the frequency exhibits the same tendency. In this manner, (16) and (17) are used, respectively, to determine the voltage, V_{ref} , and frequency, f_{ref} .

$$V_{ref} = V_0 - (K_{pq} + K_{iq}/s)(V_d - V_0) \quad (16)$$

$$f_{ref} = f_0 - \left(K_{pp} + \frac{K_{iq}}{s} \right) (f - f_0) \quad (17)$$

where f denotes the observed frequency, V_d denotes the measured voltage, s denotes the Laplace operator, and K_{pp} and K_{ip} denote, respectively, the proportional and integral gain of an active power PI regulator and the reactive power PI regulator's

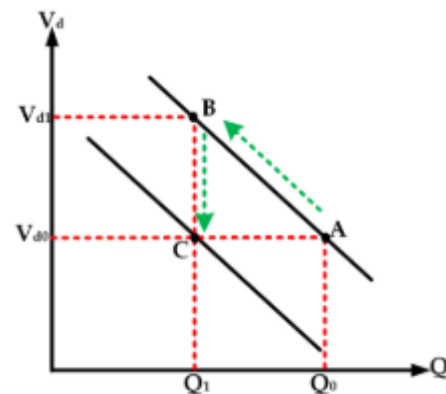


FIGURE 9 When the load varies, the controller modifies the droop characteristics to monitor the voltage.

A. EV CHARGING MODE (G2V MODE):

In this mode, the power converter functions as a rectifier, enabling the flow of energy from the three-phase grid to the electric vehicle battery.

The dual-loop feed forward decoupling technique is employed [24], consisting of the inner current loop and outside voltage control loop for the d- and q-axis current control, as illustrated in Figure 10. The first loop, known as a rapid current loop, generates

control signals (duty cycle) to regulate the current passing through the active front end. This loop is intended to limit current harmonics and react rapidly to variations in load current. The second loop, which generates the current reference (i_{dref}), is a slower voltage loop that regulates the voltage across the DC bus. This loop regulates the power factor and keeps the DC bus voltage steady. The functions of i_{dref} , i_{qref} and i_d , i_q , which are displayed in (18) and (19), can be used to express the references v_d and v_q . The proportional and integral gains are represented by K_p and K_i , respectively.

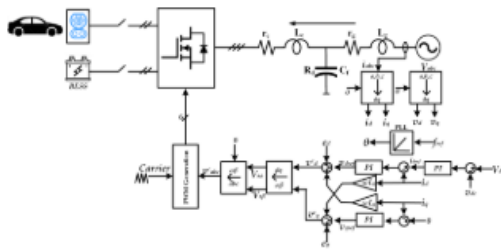


FIGURE 10. Controlling EV battery charging using feedforward decoupling

$$v_d^c = e_d + [\omega L]_g i_q - (K_p + K_i/s)(i_{dref} - i_d) \quad (18)$$

$$v_q^c = e_q + [\omega L]_g i_d - (K_p + K_i/s)(i_{qref} - i_q) \quad (19)$$

The voltage drops across the inductance of the AC side inductors is compensated for by the feedforward portion of the control method. The feedforward control determines the voltage drop across the inductance by detecting the voltage and current on the AC side. It then adds this value to the voltage reference of the voltage loop. This adjustment lowers distortion and increases the voltage control's precision.

C. EV BATTERY DISCHARGING MODE (V2G MODE):

As seen in Figure 11, the inverter adjusts the injected active and reactive power in this mode based on the main grid's voltage and frequency. The inverter uses equations (20) and (21) to determine the currents. where K'_p and K'_i are the gains from the PI controller to enhance the injected power quality, and K_P and K_Q are the droop parameters. The inverter injects the rated active and reactive power levels if the main grid's voltage and frequency are at their nominal values of 400V and 50 Hz. To preserve the stability of the main grid, the inverter's control adjusts the injected power in response to any changes in voltage or frequency [19].

$$I_{d_{blas}} = \left[(P - P_0) - \frac{1}{K_P} (f - f_0) \right] \left[K'_{pp} + \frac{K'_{ip}}{s} \right] \quad (20)$$

$$I_{q_{blas}} = \left[(Q - Q_0) - \frac{1}{K_Q} (V - V_0) \right] \left[K'_{pp} + \frac{K'_{ip}}{s} \right] \quad (21)$$

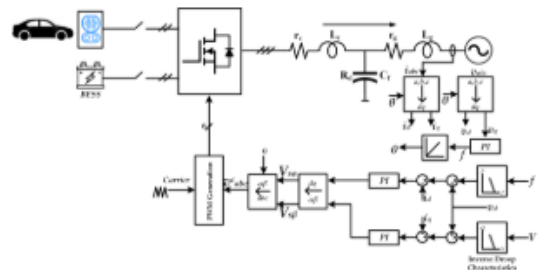


FIGURE 11 Using a grid-following droop management technique, EV battery discharge is managed to preserve grid voltage and frequency.

A. OPERATING MODE CONTROL STRATEGY:

Ongoing study is being done on a comprehensive energy management plan and how the suggested system's TCO will be affected. Figure 12 displays the total control algorithm for the EV and charging station. The method starts by gathering EV data, including the SoC of the EV battery, the voltage of

the battery, V_b , the arrival time, T_a , and the departure time, T_d . The EV will switch to grid-to-vehicle (G2V) mode if the current SoC of the EVB is less than SoC min, which is a predetermined value of charge required for emergencies. The EVB is charged with constant voltage (CV) and constant current (CC) in this mode. The charging process keeps going until SoC equals SoC max, or about 80% of SoC, the maximum value of charge. Two requirements must be met for the V2G mode to activate: the SoC must be equal to or more than the SoC max, and the EV owner must provide their agreement. Similarly, the EV user's authorization is required for V2H mode activation.

B. CONTROLLER DESIGN STRATEGY:

The architecture and control system of a single-phase LCL-type grid-connected inverter are shown in Figure 13(a). An LCL filter is used to connect a standard voltage-source inverter (VSI) for single-phase operation to the grid. The grid-side inductor (L_g), the filter capacitor (C_f), and the inverter-side inductor (L_c) make up the LCL filter. The LCL values' design is taken from [25]. Reactive power absorption of about 1% and inductor current ripple of less than 50% are taken into account when designing the LCL. The insignificant values of the equivalent series resistors for L_c and L_g are ignored in this situation. Furthermore, for calculation simplicity, the related sensor gains for grid voltage and injected grid current measurement are also ignored. The ratio of the triangle carrier wave's voltage amplitude to the dc link voltage is known as the KPWM, or PWM converter gain. The LCL filter's open loop gain can be written as (22).

$$T(s) = \frac{K_{PWM} \left(K_P + \frac{K_i}{s} \right) (1 + sR_d C_f)}{s^3 L_c L_g C_f + s^2 (L_c + L_g) R_d C_f K_{PWM} + s(L_c + L_g)} \tag{22}$$

The controller gains, K_p and K_i , are the only ones in charge of enhancing the system's dynamic

performance and stability. We'll talk about the gain tweaking approach below:

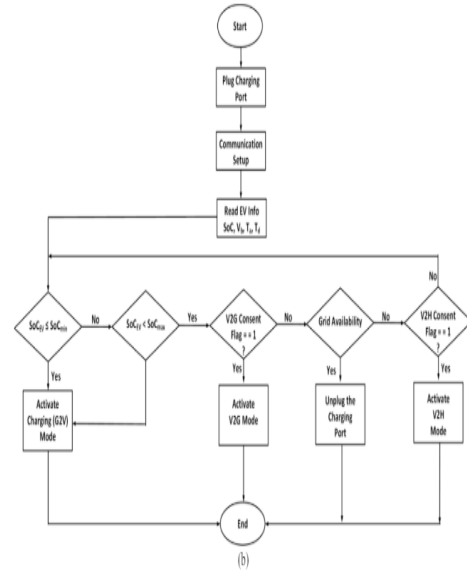


FIGURE 12 Overall control algorithm to turn on the suggested system's operating mode

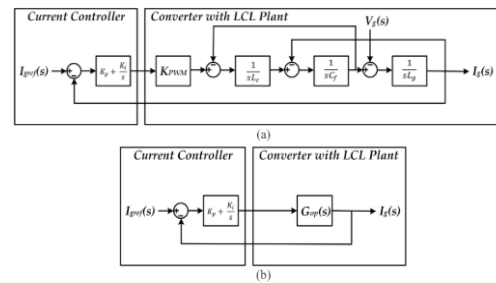


FIGURE 13. Grid-connected inverter closed-loop transfer function model with LCL filter included. (a) Controller-based converter plant transfer function; (b) closed-loop structure based on PI controller with a simplified plant function

1) PROPORTIONAL GAIN (KP) CALCULATION:

An LCL-filter based grid-connected inverter's reduced control loop topology is depicted in Figure 13(b), where $G_{op}(s)$ is the LCL open loop transfer function. One can estimate the resonant frequency (f_r) at which the system displays maximum impedance using (23), or from the bode plot of the current control loop. Likewise, the cutoff frequency

(f_c) at which the LCL filter's impedance equals the load impedance, which is usually resistive and can be either the load or the inverter's output impedance.

The crossover frequency (f_c) is usually kept below the resonance frequency (f_r) in order to efficiently minimize high frequency noise. As a result, the converter enhances the output waveform's quality by enabling the LCL filter to efficiently suppress high-frequency harmonics and noise. Additionally, the LCL filter's resonant frequency (f_r) is often limited to a range of 1/4 to 1/2 of the equivalent the inverter's switching frequency ($2 f_s$ for a unipolar PWM signal) and the lower bound of its fundamental frequency, f_0 . These restrictions reduce the possibility of resonance effects, which may result in current distortion, voltage spikes, and even component damage. Since the reactance of the filter capacitor is much bigger than that of the grid-side inductor, the capacitor branch can be regarded as open circuit for computing the size of both the frequencies below f_c and the loop gain at f_c . As a result, the filter capacitor affects and is disregarded in order to approximate $T(s)$, as stated in (24).

$$f_r = \frac{1}{2\pi} \sqrt{\frac{L_c + L_g}{L_c L_g C_f}} \quad (23)$$

$$|T(s)| \approx \frac{K_{PWM} \left(K_p + \frac{K_i}{s} \right)}{s(L_c + L_g)} \quad (24)$$

Figure 14 shows the bode diagram for the current control loop. The PI controller magnitude plot's phase shifts from -90° to 0° around crossover frequency, or f_c , and its slope changes from -20 to 0 dB. As a result, at f_c , the $T(s)$ magnitude equals unity. Furthermore, for frequencies close to or greater than the crossover frequency, the PI controller can be roughly equivalent to K_p . The result of substituting K_p and $|T(s)| = 1$ into (25) is

$$K_P \approx \left(\left[2\pi f \right]_c (L_c + L_g) \right) / K_{PWM} \quad (25)$$

It is evident from equation (25) that f_c is roughly proportional to K_p . Thus, a faster dynamic reaction is associated with a bigger K_p .

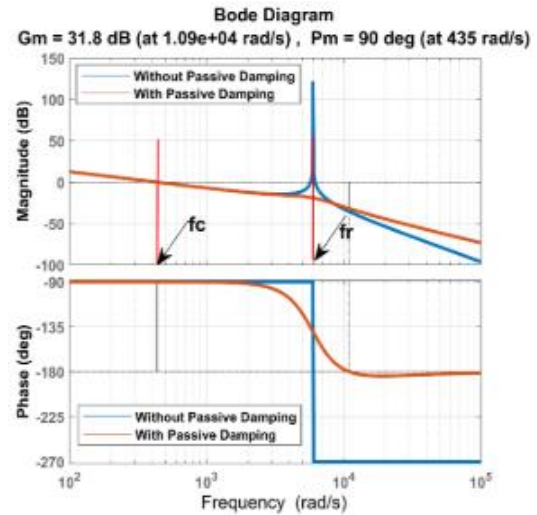


FIGURE 14 frequency response of the proposed system's present control loop.

INTEGRAL GAIN (KI) CALCULATION:

One important limitation on the grid current control system's K_i gain adjustment is the steady state error (E_{ss}). The voltage regulation's precision is related to the E_{ss} . Higher power quality and grid stability result from an inverter that is more adept at sustaining the appropriate voltage levels, as shown by a lower E_{ss} . Because the grid voltage phase was accurately determined in this study, the amplitude error (E_{ss}) is the only topic of discussion. (26) is a representation of the amplitude mistake [26].

$$|T(j2\pi f)|_{(f=f_0)} = (1/E_{ss}) \quad (26)$$

At f_0 , the $T(s)$ magnitude is around 40dB. The bode plot of the PI controller is in the -20 dB/decade slope zone since the f_0 is substantially smaller than the crossover frequency (f_c). Therefore, it is possible to ignore the proportionality constant, K_p . At f_0 , the magnitude of $T(s)$ is $K_i/(j2\pi f_0)$. By replacing $K_i/(j2\pi f_0)$ at f_0 , the (24) can be rearranged, and $|T(s)|$ yields

$$|T(j2\pi f)|_{f=f_0} \approx \frac{K_{PWM} \left(\frac{K_i}{j2\pi f_0} \right)}{j2\pi f_0 (L_c + L_g)} \quad (27)$$

By changing (26) into (27), we can express the relationship between the steady state error (E_{ss}) and the integral gain (K_i) as (28) [27].

$$K_i \geq ([40\pi] ^2 f_0^2 (E_{ss}) (L_c + L_g)) / K_{PWM} \quad (28)$$

The aforementioned expression indicates that the choice of K_i gain should be estimated using the system parameter at the fundamental frequency, f_0 , for a desired percentage value of E_{ss} . For example, for 5% E_{ss} , the $|j2\pi f|_{f=f_0}$ is 26.02dB. Because of this, K_i has a value of about 3800 for the specified system parameters. If the E_{ss} is less than 5%, then $|j2\pi f|_{f=f_0}$ ought to be more than 26.02dB. Consequently, $K_i > 3800$ must satisfy from (23), ensuring E_{ss} less than 5% even for substantial grid impedance variations. Figure 15 depicts the link between E_{ss} and K_i .

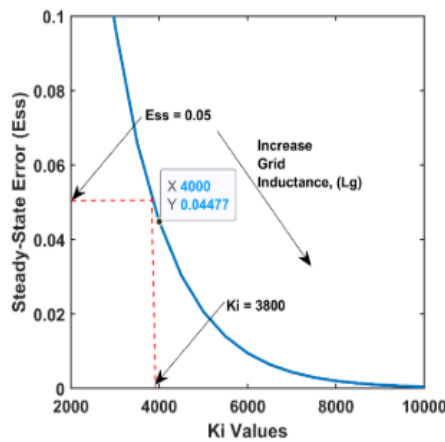


FIGURE 15. the relationship between the current control loop's integral gain (K_i) and steady-state error (E_{ss}).

V. SIMULATION RESULTS AND DISCUSSIONS:

The simulation results of the suggested bidirectional EV charging converter under the various operating circumstances mentioned in the preceding section are shown in this part. The rated power of each

individual converter is 20 kW, with a line-to-line voltage of 400V and a grid frequency of 50 Hz. Additionally, the converter can run at a maximum DC-link voltage of 800 V, meaning the operating current on the DC side cannot exceed 32 A. TABLE II below displays the converter specifications together with system parameters:

Symbols	Descriptions	Values
P	Rated power	20 kW
V_s	Supply voltage from grid	400 Vrms
V_{dc}	DC-link voltage	800 V
f_s	Switching frequency	20 kHz
f_g	Grid frequency	50 Hz
L_g	Filter inductance (grid side)	1.35 mH
C_f	Filter capacitance	50 μ F
L_c	Filter inductance (converter side)	0.961 mH
C_{dc}	DC-link capacitance	1000 μ F
R_d	Damping resistance	0.01 Ω

TABLE II CONVERTER MODULE SPECIFICATIONS AND SYSTEM PARAMETERS

It is assumed that the residential structure with its 2500 square foot (233 m²) of apartments, which include gas and hot water, is a model for the suggested system. Including highly inductive home appliances such refrigerators, air conditioners, washing machines, vacuum cleaners, clothes dryers, 5-ton central air, etc., a maximum home load of 36 kWh is taken into consideration [28]. This section describes the state space based tiny signal model. The system parameters are used to estimate the input matrix and state transition. With the help of the MATLAB/Simulink platform, the open-loop plant transfer function for the voltage and current control loop is developed from the state space model. The primary elements that determine how the system plant operates are the LCL filter parameters. As a result, the LCL filter's damping resistance and inductance—two key parameters—have a significant impact on the stability of the system controller. This paper discusses the impact of series damping resistance, R_d , on stability.

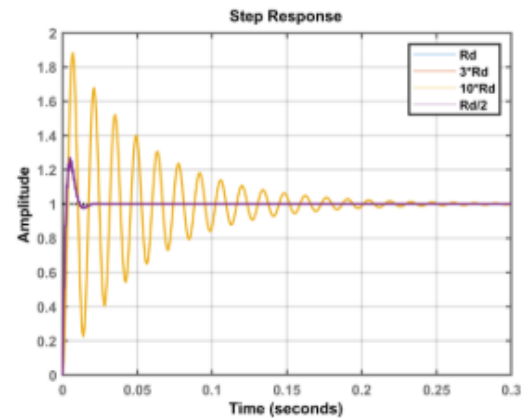
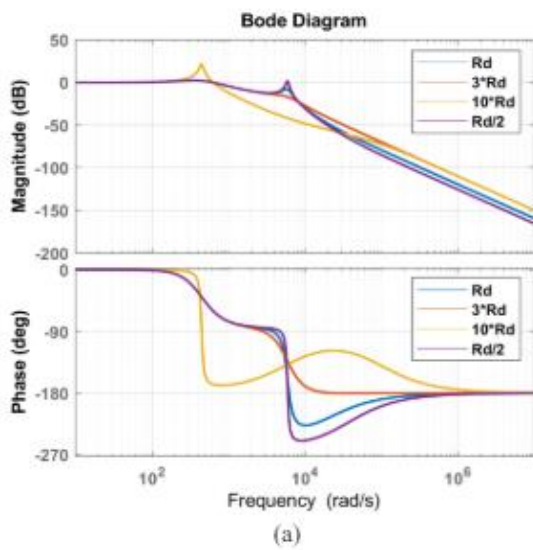
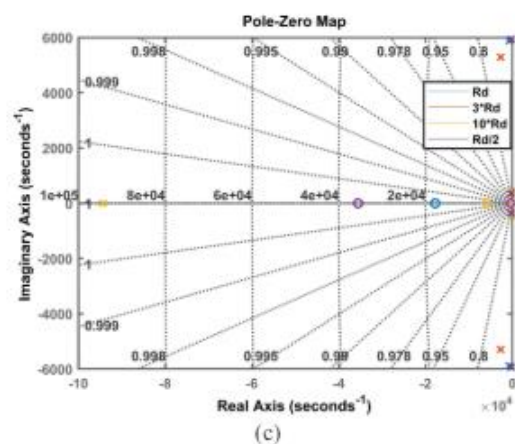
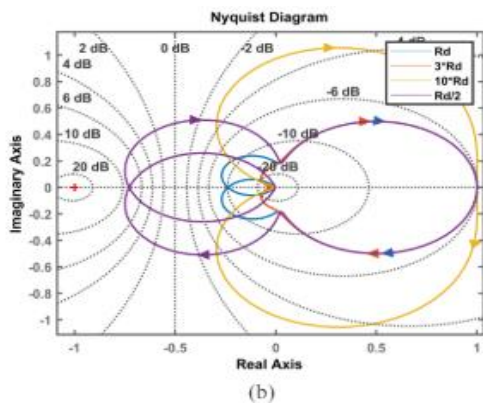


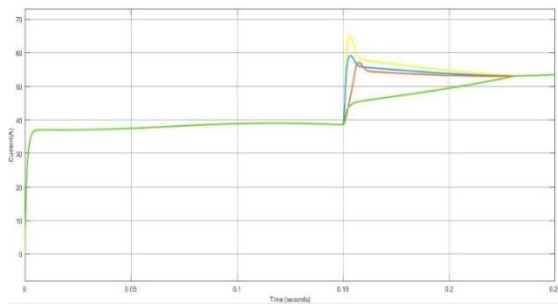
FIGURE 16. performance of the current controller loop under various load variations.



(a) Nyquist diagram, (b) Bode plot, (c) Pole-zero map, and (d) Step response

(b) The current control loop's high-frequency harmonic attenuation slope, as depicted in Figure 16(a), remains at -60 dB/dec; nevertheless, an increase in R_d causes the resonant peak frequency to occur. Additionally, it was observed that the system nearly became unstable at $10 \cdot R_d$, as indicated by the phase margin (PM) turning negative. The Nyquist plot, as depicted in Figure 16(b), guarantees a decreasing stability margin at larger R_d due to the Nyquist circle's movement towards the $(-1,0)$ point in the complex plane. The poles persist on the left side until the $10 \cdot R_d$ variation, as illustrated by the pole zero map in Figure 16(c). As a result, at greater R_d , the system steady-state response depicted in Figure 16(d) starts to oscillate.

The frequency response of the voltage control loop exhibits a similar phenomenon. By limiting the system parameters, these observations aid in preventing unstable operating points. The system parameters are used to create the tiny signal model. MATLAB/Simulink software is also used to validate the response of the tiny signal model with the high-fidelity model. Figure 17 displays the grid-connected inverter's dq-axis current response.



(a)



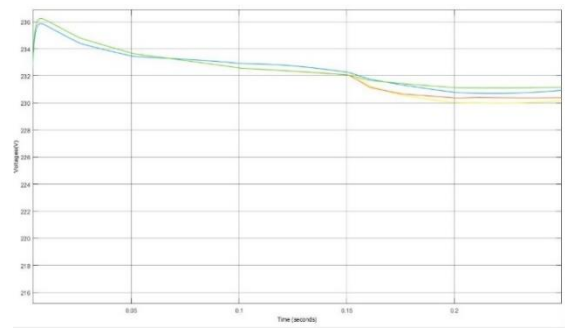
(b)

FIGURE 17. The performance comparison of the dq-axis current profile for the HiFi and small signal models in V2H mode, including the RL load transition at $t=0.15$ seconds. (a) d-axis current. (b) q-axis current

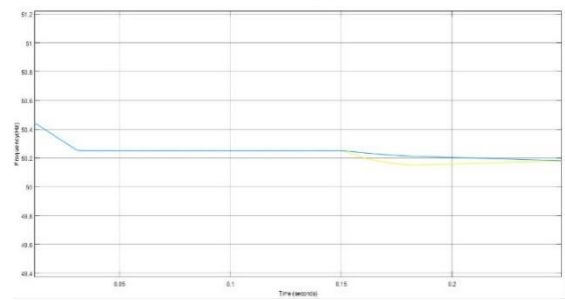
This work considers the single-phase residential RL load. Up to $t=0.15$ seconds, the load demand is estimated at roughly 26kW and 23kVAR. After that, until $t=0.25$ seconds, the load is increased to 38kW and 36kVAR. The charging station powers the load in V2H mode by acting as a standalone off-grid inverter. Either the solar PV array or the electric vehicle battery storage system's DC power is converted by the inverter. Up to $t=0.15$ sec, the load current requirement is originally 75A at 400V (L-L).

Following that, as the RL load increased, the current demand rose by about 55A. There is a 3Ω load resistance and a 9.5mH inductance, respectively. Figure 17(a) displays the system d-axis current response via I_d for both the small-signal and high-fidelity models.

The small-signal model must be observed to operate exactly like the high-fidelity model up to $t=0.15$ sec, during which time each converter is supplying 38A. After $t=0.15$ seconds, the transient response changes during the load changeover and stabilizes about $t=0.23$ seconds or such.



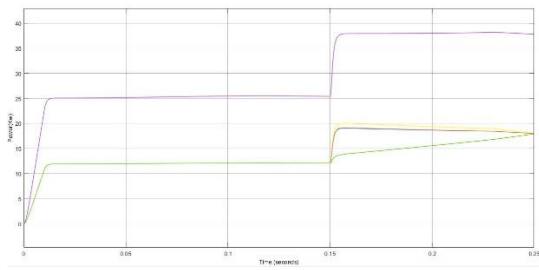
(a)



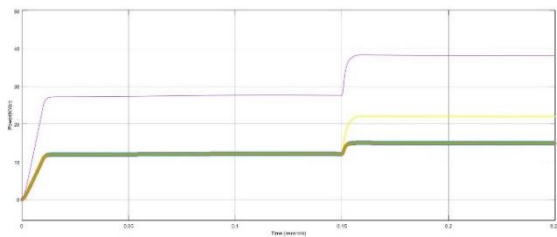
(b)

The transient behaviour of the circuit breaker and switching arc causes the transient response during load switching to differ from the high-fidelity model. However, because the contactor is still closed, this occurrence is not initially noticed. An additional noteworthy finding is that, for every converter, the overshoot of the small-signal model response is substantially less than the high-fidelity model response, by about 15A. Therefore, real-time control systems can be efficiently designed using the transfer functions of this tiny signal model. Figure 17(b) shows a similar dynamic response of the q-axis current, which helps to meet the reactive power requirement. Conversely, Figure 18(a)'s voltage response illustrates how the voltage control maintains the supply voltage to the load at 230V (L-N).

As the reactive power demand rises, the load voltage produced by the inverter decreases. Figure 18(b) displays the response of the load frequency. As the active power increases, the load frequency decreases. Up to $t=0.15$ sec, the frequency reference for both converters is approximately 50.25 Hz, which is produced using the P-f droop characteristics mentioned in (10) and (11).



(a)

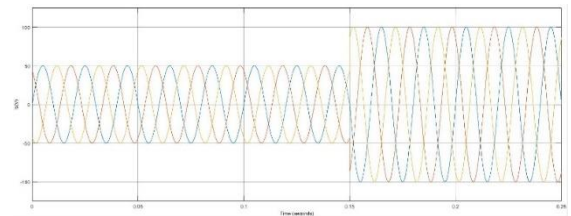
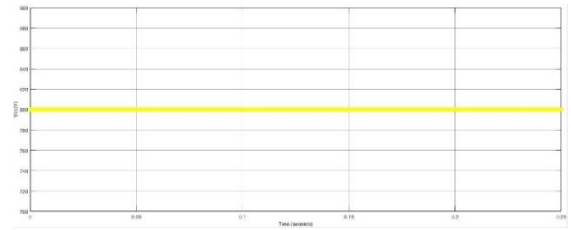


(b)

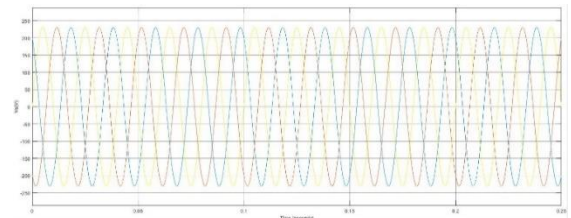
FIGURE 19. Performance comparison of the HiFi and small signal models' active and reactive power profiles during V2H mode, including the RL load transition at t=0.15 seconds. (a) d-axis voltage, (b) load frequency

FIGURE 19 Active and reactive power profile performance comparison for HiFi and small signal model incorporating RL load transition at t=0.15 sec; (a) D-axis voltage; (b) load frequency during V2H mode

Figure 20 shows the battery performance profile (a). The battery's state of charge (SoC) ought to be sufficiently high to meet the current demand needed by the household load. During V2G, the battery SoC drops, and the rate of fall is high after the load requirement increases at t=0.15 seconds. As seen in Figure 20(a), the pre-charged amount of the dc-link capacitor keeps the dc link voltage at 800V. When the load demand is around 26kW, the battery provides 38A of current.



(a)



(b)

FIGURE 20. Performance of the DC and AC sides for V2H mode, including the RL load transition at t=0.15 seconds. The grid's voltage, current, and THD profile during V2H service; (a) the performance of the EV battery (SoC, voltage, and current).

Figure 20(b) shows the voltage and current waveforms on the AC side during V2H mode. About 50 Arms of load absorption are required for a 36kW load requirement at 230V (P-N) and 3% THD. The THD likewise drops to less than 2% as the load requirement rises to 38kW. At high power distribution to households, the quality of the power is superior. Throughout V2H, there is a lot of output voltage ripple. The main cause is that the switching frequency was chosen incorrectly. For V2H mode, the switching frequency of 20 kHz might be too high. Furthermore, the AC voltage ripple cannot be smoothed out by the filter capacitor's size.

VI. CONCLUSIONS

This work thoroughly examines the design, control, and validation features of an integrated electric vehicle (EV) charging station for residential usage, incorporating a fuzzy logic controller for enhanced performance. The station features a grid-interfacing inverter that facilitates PV installation, energy storage, and buffer power delivery. The model, controlled by fuzzy logic, is compared to the HiFi model, showing a performance error of only 0.46%. However, during load transition phases, the performance error increases to 5–10%, taking about 1.5 seconds to stabilize. In V2H mode with an RL load supply, the THD is about 5%. The fuzzy logic-controlled charging and V2G controllers maintain the dc-link voltage around 750V during the steady-state phase with less than 1% voltage ripple, and from 370V to 364V during V2G. The dc-link voltage stabilizes within 0.3 seconds, with an acceptable voltage ripple (<1%). Experimental findings demonstrate that the proposed fuzzy logic solution effectively reduces peak demand while enhancing energy efficiency and power quality. The charging efficiency is approximately 87% at a 35% initial SoC with 6.3 kW of grid power drawn. When the battery returns energy to the grid at a rate of 8.6kW on the AC side, with 8.77kW of battery power input, the V2G efficiency reaches almost 94% at a 55% initial SoC. This fuzzy logic-based solution is easily integrated into the existing power grid architecture and is scalable, offering valuable insights into building an integrated EV charging station for residential use, contributing to more intelligent and sustainable energy systems.

$$A_{ii} = \begin{bmatrix} \frac{R_1(L_1 + M_{1p})}{K_1} & \frac{R_2M_{1p}}{K_1} & \frac{R_2M_{1p}}{K_1} & \frac{R_1(L_1 + M_{1p})}{K_1} & \frac{R_2M_{1p}}{K_1} & \frac{R_2M_{1p}}{K_1} \\ -\omega + \frac{R_2M_{1p}}{K_1} & \frac{R_1(L_1 + M_{1p})}{K_1} & \frac{R_2M_{1p}}{K_1} & \frac{R_2M_{1p}}{K_1} & \frac{R_1(L_1 + M_{1p})}{K_1} & \frac{R_2M_{1p}}{K_1} \\ \frac{R_2M_{1p}}{K_1} & \frac{R_2M_{1p}}{K_1} & \frac{R_1(L_1 + M_{1p})}{K_1} & \frac{R_2M_{1p}}{K_1} & \frac{R_2M_{1p}}{K_1} & \frac{R_1(L_1 + M_{1p})}{K_1} \\ \frac{R_2M_{1p}}{K_1} & \frac{R_2M_{1p}}{K_1} & \frac{R_2M_{1p}}{K_1} & \frac{R_1(L_1 + M_{1p})}{K_1} & \frac{R_2M_{1p}}{K_1} & \frac{R_2M_{1p}}{K_1} \\ \frac{R_2M_{1p}}{K_1} & \frac{R_2M_{1p}}{K_1} & \frac{R_2M_{1p}}{K_1} & \frac{R_2M_{1p}}{K_1} & \frac{R_1(L_1 + M_{1p})}{K_1} & \frac{R_2M_{1p}}{K_1} \\ \frac{R_2M_{1p}}{K_1} & \frac{R_2M_{1p}}{K_1} & \frac{R_2M_{1p}}{K_1} & \frac{R_2M_{1p}}{K_1} & \frac{R_2M_{1p}}{K_1} & \frac{R_1(L_1 + M_{1p})}{K_1} \end{bmatrix}$$

APPENDIX STATE-SPACE MODEL MATRICES

$$A = \begin{bmatrix} A_{11} & 0 & \dots & 0 & A_{21} & 0 & \dots & 0 & A_{31} \\ 0 & A_{12} & \dots & 0 & 0 & A_{22} & \dots & 0 & A_{32} \\ \vdots & \vdots & \ddots & \vdots & \vdots & \vdots & \ddots & \vdots & \vdots \\ 0 & 0 & \dots & A_{1n} & 0 & 0 & \dots & A_{2n} & A_{3n} \\ A_{41} & 0 & \dots & 0 & A_{51} & 0 & \dots & 0 & 0 \\ 0 & A_{42} & \dots & 0 & 0 & A_{52} & \dots & 0 & 0 \\ \vdots & \vdots & \ddots & \vdots & \vdots & \vdots & \ddots & \vdots & \vdots \\ 0 & 0 & \dots & A_{4n} & 0 & 0 & \dots & A_{5n} & 0 \\ A_{61} & A_{62} & \dots & A_{6n} & 0 & 0 & \dots & 0 & -\frac{K_{batt}}{nC_{dc}} \end{bmatrix}$$

$$B = \begin{bmatrix} B_{11} & 0 & \dots & 0 & B_{21} \\ 0 & B_{12} & \dots & 0 & B_{22} \\ \vdots & \vdots & \ddots & \vdots & \vdots \\ 0 & 0 & \dots & B_{1n} & B_{2n} \\ 0 & 0 & \dots & 0 & 0 \\ 0 & 0 & \dots & 0 & 0 \\ \vdots & \vdots & \ddots & \vdots & \vdots \\ 0 & 0 & \dots & 0 & 0 \\ B_{31} & B_{32} & \dots & B_{3n} & 0 \end{bmatrix}$$

$$C = [I]^{(6n+3n+1) \times (6n+3n+1)}$$

$$D = [0]^{(6n+3n+1) \times (3n+3)}$$

$$A_{ii} = \begin{bmatrix} \frac{(L_1 + M_{1p})}{K_1} & \frac{M_{1p}}{K_1} & \frac{M_{1p}}{K_1} \\ \frac{M_{1p}}{K_1} & \frac{(L_1 + M_{1p})}{K_1} & \frac{M_{1p}}{K_1} \\ \frac{M_{1p}}{K_1} & \frac{M_{1p}}{K_1} & \frac{(L_1 + M_{1p})}{K_1} \end{bmatrix} \quad A_{ii} = \begin{bmatrix} \frac{S_1(L_1 + M_{1p}) - S_1M_{1p} - S_1M_{1p}}{K_1} & \frac{S_1M_{1p}}{K_1} & \frac{S_1M_{1p}}{K_1} \\ \frac{S_1M_{1p}}{K_1} & \frac{S_1(L_1 + M_{1p}) - S_1M_{1p} - S_1M_{1p}}{K_1} & \frac{S_1M_{1p}}{K_1} \\ \frac{S_1M_{1p}}{K_1} & \frac{S_1M_{1p}}{K_1} & \frac{S_1(L_1 + M_{1p}) - S_1M_{1p} - S_1M_{1p}}{K_1} \end{bmatrix} \quad A_{ii} = \begin{bmatrix} \frac{1}{C_1} & 0 & 0 & \frac{1}{C_1} & 0 & 0 \\ 0 & \frac{1}{C_1} & 0 & 0 & \frac{1}{C_1} & 0 \\ 0 & 0 & \frac{1}{C_1} & 0 & 0 & \frac{1}{C_1} \end{bmatrix}$$

$$A_{ii} = \begin{bmatrix} -\omega & 0 \\ \omega & 0 \\ 0 & 0 \\ 0 & 0 \end{bmatrix} \quad A_{ii} = \left[\frac{S_1}{nC_{dc}} \quad -\frac{S_1}{nC_{dc}} \quad -\frac{2S_1}{nC_{dc}} \quad 0 \quad 0 \quad 0 \right]$$

$$B_{ii} = \begin{bmatrix} \frac{V_1(L_1 + M_{1p})}{K_1} & \frac{V_1M_{1p}}{K_1} & \frac{V_1M_{1p}}{K_1} \\ \frac{V_1M_{1p}}{K_1} & \frac{V_1(L_1 + M_{1p})}{K_1} & \frac{V_1M_{1p}}{K_1} \\ \frac{V_1M_{1p}}{K_1} & \frac{V_1M_{1p}}{K_1} & \frac{V_1(L_1 + M_{1p})}{K_1} \\ 0 & 0 & 0 \\ 0 & 0 & 0 \\ 0 & 0 & 0 \end{bmatrix} \quad B_{ii} = \begin{bmatrix} 0 & 0 & 0 \\ 0 & 0 & 0 \\ \frac{(L_1 + nL_1 + M_{1p})}{K_1} & \frac{M_{1p}}{K_1} & \frac{M_{1p}}{K_1} \\ \frac{M_{1p}}{K_1} & \frac{(L_1 + nL_1 + M_{1p})}{K_1} & \frac{M_{1p}}{K_1} \\ \frac{M_{1p}}{K_1} & \frac{M_{1p}}{K_1} & \frac{(L_1 + nL_1 + M_{1p})}{K_1} \\ 0 & 0 & 0 \end{bmatrix}$$

$$B_{11,2, \dots, n-1} = \left[\frac{I_d}{nC_{dc}} \quad -\frac{I_d}{nC_{dc}} \quad -\frac{I_d}{nC_{dc}} \right] \quad B_{1n} = \left[\frac{I_d}{nC_{dc}} \quad -\frac{I_d}{nC_{dc}} \quad -\frac{(n-1)I_d}{nC_{dc}} \right]$$

$$K_1 = (L_1 + 2M_{1p})(L_1 - M_{1p}) \quad K_2 = (L_1 + nL_1 + 2M_{1p})(L_1 + nL_1 - M_{1p})$$

REFERENCES:

- [1] “Brussels transit company STIB will replace 411 diesel buses by 2030” Brussels Times, 23 Apr, 2023. Available on -transit-company-stib-will-replace-411-diesel-buses-by-2030 [accessed on 28 Feb,2023]
- [2] “De Lijn to buy up to 1,250 electric buses within 6 years “Available on 1250-electric-buses-within-six-years/ [accessed on 28 Feb, 2023].
- [3] Max Molliere “E-Vans: Cheaper, Greener Andin demand” Transport Environment, March 2022. Available on content/uploads/2022/03/2022_03_van_TCO_report-1.pdf [accessed on 28 Feb, 2023].

- [4] Julian Conzade, Florian Nägele, Swarna Ramanathan, and Patrick Schaufuss “Europe’s EV opportunity—and the charging infrastructure needed to meet it” McKinsey & Company, Nov 2022. Available on <https://www.mckinsey.com/industries/automotive-and-assembly/our-insights/europes-ev-opportunity-and-the-charging-infrastructure-needed-to-meet-it> [accessed on 28 Feb 2023].
- [5] Ahmad, A.; Khalid, M.; Ullah, Z.; Ahmad, N.; Aljaidi, M.; Malik, F.A.; Manzoor, U. Electric Vehicle Charging Modes, Technologies and Applications of Smart Charging. *Energies* 2022, 15, 9471.
- [6] Johnson, J.; Berg, T.; Anderson, B.; Wright, B. Review of Electric Vehicle Charger Cybersecurity Vulnerabilities, Potential Impacts, and Defenses. *Energies* 2022, 15, 3931
- [7] “Solar Energy Deployment in EU 2030: Global Energy Crisis Series” published in ECO Green Energy. Available Online: <https://www.ecogreenenergy.com/solar-energy-deployment-in-eu-2030-global-energy-crisis/> (accessed on 12 March 2023)
- [8] “New analysis reveals over 1 million European homes are solar battery-powered” published in Solar Power Europe. Available Online: (accessed on 12 March 2023).
- [9] “Electric cars as buffer storage for solar power: Infineon and Delta enable bidirectional charging at home” press released by Infineon in Jul 2022. Available online: <https://www.infineon.com/cms/en/about-infineon/press/press-releases/2022/INFIPIC202207-105.html>(accessed on 12 March 2023).
- [10] “Fast EV Charging” Infineon (DC Wall box). Available online: <https://www.infineon.com/cms/en/applications/industrial/ev-charging/dc-wallbox/> (accessed on 13 March 2023).
- [11] M. A. H. Rafi and J. Bauman, "A Comprehensive Review of DC Fast-Charging Stations with Energy Storage: Architectures, Power Converters, and Analysis," in *IEEE Transactions on Transportation Electrification*, vol. 7, no. 2, pp. 345-368, June 2021
- [12] G. Rituraj, G. R. C. Mouli and P. Bauer, "A Comprehensive Review on Off-Grid and Hybrid Charging Systems for Electric Vehicles," in *IEEE Open Journal of the Industrial Electronics Society*, vol. 3, pp. 203-222, 2022.
- [13] Worighi, I.; Geury, T.; El Baghdadi, M.; Van Mierlo, J.; Hegazy, O.; Maach, A. “Optimal Design of Hybrid PV-Battery System in Residential Buildings: End-User Economics, and PV Penetration” *Appl. Sci.* 2019, 9, 1022. <https://doi.org/10.3390/app9051022/>
- [14] ADS-TEC Energy white paper published in Business wire on Jul 2022. Available Online: [Technology-Can-Meet Increasing-Demands-and-Save-Charge-Network-Operators-Up-to-30-in-TCO#:~:text=TCO%20%7C%20Business%20Wire,New%20Research%20Shows%20How%20Ultra%2DFast%2C%20Battery%2DBuffered%20EV,Up%20to%2030%25%20in%20TCO](https://www.businesswire.com/news/home/202207050052767/en/ADS-TEC-Technology-Can-Meet-Increasing-Demands-and-Save-Charge-Network-Operators-Up-to-30-in-TCO#:~:text=TCO%20%7C%20Business%20Wire,New%20Research%20Shows%20How%20Ultra%2DFast%2C%20Battery%2DBuffered%20EV,Up%20to%2030%25%20in%20TCO) (accessed on 12 March 2023) s/
- [15] Huber, D.; De Clerck, Q.; De Cauwer, C.; Sapountzoglou, N.; Coosemans, T.; Message, M. “Vehicle to Grid Impacts on the Total Cost of Ownership for Electric Vehicle Drivers” *World Electric Vehicle Journal*, 2021, 12, 236.
- [16] G. R. C. Mouli, J. Kaptein, P. Bauer and M. Zeman, "Implementation of dynamic charging and V2G using Chademo and CCS/Combo DC charging standard," 2016 IEEE Transportation Electrification Conference and Expo (ITEC), Dearborn, MI, USA, 2016, pp. 1-6.

- [17] Jaman, S.; Verbrugge, B.; Garcia, O.H.; Abdel-Monem, M.; Oliver, B.; Geury, T.; Hegazy, O. Development and Validation of V2G Technology for Electric Vehicle Chargers Using Combo CCS Type 2 Connector Standards. *Energies* 2022, 15, 7364.
- [18] "Off Grid Solar System for Home with Battery Backup, 2023" published in Ken brook Solar. Available Online: [off-grid-solar-power-plants](https://www.kenbrook.com/off-grid-solar-power-plants) (accessed on 12 March 2023)
- [19] J. Svarc "Home Solar EV Charging" Published Clean Energy Reviews on March 10 2023. Available Online: (accessed on July 11 2023)
- [20] "What is the average electricity and gas consumption in the Brussels region" published by Sibelga Energguide. Available Online:(accessed in)
- [21] Liberos, M.; González-Medina, R.; Patrao, I.; Garcerá, G.; Figueres, E. "A Control Scheme to Suppress Circulating Currents in Parallel-Connected Three-Phase Inverters" *Electronics* 2022, 11, 3720.
- [22] Liberos, M.; González-Medina, R.; Garcerá, G.; Figueres, E. Modelling and Control of Parallel-Connected Transformerless Inverters for Large Photovoltaic Farms. *Energies* 2017, 10, 1242.
- [23] Sal y Rosas, D.; Zarate, A. Single-Phase Grid-Forming Strategy with Power Decoupling Implementation for Electrolytic-Capacitor-Free EV Smart Battery Charger. *Energies* 2023, 16, 894.
- [24] H. Rasool, A. Zhaksylyk, S. Chakraborty, M. E. Baghdadi and O. Hegazy, "Optimal Design Strategy and Electro-Thermal Modelling of a High-Power Off-Board Charger for Electric Vehicle Applications," 2020 Fifteenth International Conference on Ecological Vehicles and Renewable Energies (EVER), Monte-Carlo, Monaco, 2020, pp. 1-8.
- [25] S. Sen, K. Yenduri and P. Sensarma, "Step-by-step design and control of LCL filter base three phase grid-connected inverter," 2014 IEEE International Conference on Industrial Technology (ICIT), Busan, Korea (South), 2014, pp. 503-508
- [26] M.B. Saïd-Romdhane, M.W. Naouar, I. Slama-Belkhdja, "Systematic design method for PI controller with Virtual Resistor-based Active Damping of LCL filter", *Global Energy Interconnection*, Volume 1, Issue 3, 2018, Pages 319-329, ISSN 2096-5117.
- [27] C. Bao, X. Ruan, X. Wang, W. Li, D. Pan and K. Weng, "Step-by-Step Controller Design for LCL-Type Grid-Connected Inverter with Capacitor-Current-Feedback Active-Damping," in *IEEE Transactions on Power Electronics*, vol. 29, no. 3, pp. 1239-1253, March 2014
- [28] "How much does a standby generator cost to install?" Buckeye Power System. Available Online: <https://buckeyepowersystems.com/pages/how-much-does-a-standby-generator-cost-to-install> [accessed on 28 Feb, 2023].
- [29] J. Saleem "Summary of major recorded power outages ground Europe in past 20 years" GCCIA, April 4, 2023. Available online: outages-around-europe-20-jamshed-saleem/ (accessed on 25 July 2023)
- [30] Eugene Castillo "Turning Disaster to the Opportunity: the Nissan Leaf" Octopus: Electric Vehicle, April 2019. Available online: <https://octopusev.com/ev-hub/turning-disaster-to-opportunity-the-nissan-leaf> (accessed on 25 July 2023)
- [31] Bowen, J. Engelhardt, T. Gabderakhmanova, M. Marinelli and G. Rohde, "Battery Buffered EV Fast Chargers on Bornholm: Charging Patterns and Grid Integration," 2022 57th International Universities Power Engineering Conference (UPEC), Istanbul, Turkey, 2022, pp. 1-6.
- [32] Dubarry. M "Electric vehicle battery durability and reliability under electric utility grid operations"

EVTC project report 8, Hawaii Natural Energy Institute, May 2017.

[33] Villante, C.; Ranieri, S.; Duronio, F.; De Vita, A.; Anatone, M. An Energy-Based Assessment of Expected Benefits for V2H Charging Systems through a Dedicated Dynamic Simulation and Optimization Tool. *World Electr. Veh. J.* 2022, 13, 99.